

Journal of Experimental Nanoscience

ISSN: 1745-8080 (Print) 1745-8099 (Online) Journal homepage: https://www.tandfonline.com/loi/tjen20

Effect of platinum doping on the structural and electrical properties of SnO_2 thin films

Tarık Asar, Burak Korkmaz & Süleyman Özçelik

To cite this article: Tarık Asar, Burak Korkmaz & Süleyman Özçelik (2016) Effect of platinum doping on the structural and electrical properties of SnO_2 thin films, Journal of Experimental Nanoscience, 11:16, 1285-1306, DOI: 10.1080/17458080.2016.1212408

To link to this article: https://doi.org/10.1080/17458080.2016.1212408

Published online: 02 Aug 2016.

Submit your article to this journal

Article views: 1054

View related articles

View Crossmark data

Citing articles: 9 View citing articles

Full Terms & Conditions of access and use can be found at
https://www.tandfonline.com/action/journalInformation?journalCode=tjen20

JOURNAL OF EXPERIMENTAL NANOSCIENCE, 2016
VOL. 11, NO. 16, 1285–1306
http://dx.doi.org/10.1080/17458080.2016.1212408

Taylor & Francis
Taylor & Francis Group

Effect of platinum doping on the structural and electrical properties of SnO_2 thin films

Tarık Asar [a,b], Burak Korkmaz[a,b] and Süleyman Özçelik[a,b]

[a]Faculty of Science, Department of Physics, Gazi University, Ankara, Turkey; [b]Photonics Application and Research Center, Gazi University, Ankara, Turkey

ABSTRACT

The investigation of Pt doping effect on the structural and electrical properties of SnO_2 thin films was aimed in this study. For this purpose, the polycrystalline pure and Pt-doped SnO_2 thin films were deposited onto n-type silicon substrate and the Pt sputter power was varied as 0 (un-doped), 2, 5 and 7 W by using radio frequency confocal sputtering system. The structural properties of the samples were analysed by X-ray diffraction measurements. The structural results show that the 5 W Pt-doped SnO_2 sample has better crystallinity than the other samples. The results of the electrical measurements as current–voltage, capacitance–voltage and conductance–voltage were also obtained and discussed in detail for fabricated diodes. The analysis of electrical characteristics shows that the use of different Pt doping has significant effect on electrical properties of such devices. The study also provides an improved supplemental understanding to the related technologies which use Pt-doped SnO_2 materials.

ARTICLE HISTORY
Received 2 April 2016
Accepted 8 July 2016

KEYWORDS
SnO_2; thin films; XRD; Schottky barrier diode; electrical properties

1. Introduction

Transparent conductive oxide materials have attracted significant interest due to their prospective applications in electro-optic and electrochemical devices.[1] Among them, SnO_2 has been extensively used as a n-type semiconductor material which exhibits a fairly high electrical conductivity (10^3 S/cm), along with a direct wide bandgap (3.6 eV).[2,3] It has also unrivalled characteristics such as high transmittance in the ultraviolet-visible region and high reflectance in infrared region, high electrical conductivity, high melting point, metal-like conductivity, absence of toxicity, easy doping, easy tailoring and abundance in nature.[4,5] Thus, SnO_2 has been used in a number of applications such as electrode materials in solar cells,[6] transistors,[7] light emitting diodes,[8] flat panel displays,[9] gas sensors,[10] special catalysts,[11] high density energy storage material,[12] conductive film,[13] high performance capacitor,[14] dynamic random-access memory (RAM),[15] rechargeable lithium batteries,[16] resistors,[17] transparent heaters,[18] electrode ceramics [19] and antistatic coatings.[20]

CONTACT Tarık Asar trkasar@gazi.edu.tr

© 2016 Informa UK Limited, trading as Taylor & Francis Group

It is clearly seen from the reported results that the properties of the films and devices are strongly influenced by the method and the conditions of the deposition.[21] Thus, the deposition method choosing is quite important. In the literature, the pure and doped SnO_2 thin films have been obtained by using a variety of techniques such as chemical vapour deposition,[22] physical vapour deposition,[23] pulsed laser deposition,[24] spray pyrolysis,[25] hydrothermal method,[26] sol-gel method,[27] evaporation,[28] co-precipitation [29] and sputtering.[30] In this study, a sputtering method was chosen due to the fewer pinholes, higher purity, better adhesive quality, simpler preparation and lower cost than others.[2]

The electrical properties of the SnO_2 based devices such as the selectivity, stability, sensitivity and detecting efficiency can be improved with the adjusting of nanostructured coatings.[21] These properties can also be enhanced by doping pure SnO_2 with small amounts of noble metals such as Pt, Pd and Bi dispersed on the surface of a semiconductor.[31−33] The results of doping many d-block transition metals and rare earth elements in SnO_2 have been reported in literature.[34−36] The results of tailoring electrical properties of this non-stoichiometric 4*d* metal oxide depend on the doping, grain size, pore and surface defects. Additionally, the detecting efficiency of SnO_2 is based on its electrical property changes that are mainly depended on the homogeneity, elemental composition, point and oxygen defects distribution, chemisorbed oxygen species and oxygen vacancies of the film.[37−41] Moreover, many researchers have studied the dielectric behaviour of SnO_2 nanostructures which is concerned with the storage and dispensation of electric and magnetic energy.[42] SnO_2 nanostructures possess ultrahigh dielectric constant in the low frequency region.[43] On this basis, a detailed study on the structural and electrical properties of the SnO_2 thin films is of great importance to develop SnO_2 devices.[44]

In this paper, the Pt doping effect was investigated on the structural and electrical properties of SnO_2 thin films. For this purpose, the Pt sputter power was varied as 0 (undoped), 2, 5 and 7 W. The SnO_2 thin films were deposited onto n-type silicon substrate by using radio frequency confocal sputtering (co-sputtering) system at room temperature. The structural parameters as the crystal quality, grain size, dislocation density and strain were determined by X-ray diffraction (XRD) measurements. After that, the samples were fabricated as the Au/Pt:SnO_2/n-Si/Au Schottky barrier diodes (SBDs). The electrical properties of the Au/Pt:SnO_2/n-Si/Au SBDs were obtained by using current−voltage ($I-V$), capacitance−voltage ($C-V$) and conductance−voltage ($G/\omega-V$) data. After detailed investigation on the properties of SnO_2 thin films, it can be said that the present study effectuates an important contribution to the literature about the Pt-doped SnO_2 thin films and its related device applications.

2. Experimental details

Au/Pt:SnO_2/n-Si/Au SBDs were fabricated on the phosphorus doped (n-type) Si substrates with 380 ± 25 μm thickness, (100) orientation and 1−10 Ωcm resistivity. Prior to the fabrication, 2″ n-type Si substrate was decreased in organic solvent of $CHClCClL_2$, CH_3COOH and CH_3OH, etched in a sequence of H_2SO_4 and H_2O_2, 25% HF, a solution of 7 HNO_3:1 HF:40 H_2O, 25% HF and finally quenched in deionised water with resistivity of 18 MΩcm for a prolonged time.[45] The fabrication process can be successively separated into three parts as ohmic contact formation, SnO_2 deposition and Schottky contact

Table 1. The identification of the Pt:SnO_2/n-Si structures.

		Sputter power (W)		Deposition		
Sample	Structure	SnO_2	Pt	Temperature (°C)	Pressure (mtorr)	Thickness (nm)
S001	Pt:SnO_2/n-Si	50	0	22	30	99
S002	Pt:SnO_2/n-Si	50	2	22	30	101
S003	Pt:SnO_2/n-Si	50	5	22	30	100
S004	Pt:SnO_2/n-Si	50	7	22	30	101

formation. The back side of substrate was mounted onto the stainless steel holders and loaded into the magnetron co-sputtering system (Nanovak NVTS-500). The Au ohmic contact with 200 ± 1 nm thickness was then formed by deposition of high purity gold (Au) (99.999%) at 400 °C under 4.8×10^{-3} mbar vacuum and the substrate was annealed at 360 °C to achieve good ohmic contact behaviour. After that, the substrate was cut into the 1 cm^2 pieces and all pieces were cleaned with acetone and ethanol. The substrates were separately replaced to upper surface right after the cutting and cleaning step. After all, as seen from Table 1, un-doped and Pt-doped SnO_2 thin films with 100 ± 1 nm thickness were deposited onto the upper surface of the substrates by using high purity (99.995%) SnO_2 target at room temperature. The film thickness was also confirmed by stylus type profilometer. In order to investigate the Pt doping effect on the properties of the SnO_2 thin films, the Pt sputter power was varied as 0 (un-doped), 2, 5 and 7 W. The other deposition parameters such as SnO_2 sputter power, temperature, pressure, argon flow and target distance were kept constant at whole depositions. Thus, they were called as S001, S002, S003 and S004 and given in Table 1. In this way, the Pt:SnO_2/n-Si structures were ready for their characterisations and fabrications.

After the deposition processes, the structural properties of the samples were analysed by a high resolution X-ray diffractometer (D-8 Bruker). After that, the samples were fabricated for the electrical characterisations of the Au/Pt:SnO_2/n-Si/Au SBDs. The 1 mm dot-shaped Au rectifier contacts with 150 ± 1 nm thickness were formed onto SnO_2 thin films by the deposition of high purity (99.999%) Au at room temperature. In this way, the Au/Pt:SnO_2/n-Si/Au SBDs were ready for determining their electrical characterisations. Schematic representation of fabricated SBD was given in Figure 1.

The electrical properties of the Au/Pt:SnO_2/n-Si/Au SBDs were investigated using $I-V$, $C-V$ and $G/\omega-V$ data. These data were obtained by using a semiconductor parameter analyser (Keithley 4200) and an impedance analyser (HP 4192 A LF) system. The $C-V$ and $G/\omega-V$ measurements were achieved in the frequency range of 100 Hz−1 MHz at room temperature.

3. Results and discussion

3.1. Structural properties

The ω-2θ XRD patterns of the samples were shown in Figure 2. All the observed diffraction peaks agree well with the tetragonal structure of SnO_2 from Joint Committee of Powder Diffraction Standards (JCPDS) Card No. 41-1445. As seen from Figure 2, the high intense peak comes from n-Si substrate while the other peaks that belong to the SnO_2, SnO, SiO_2 and Pt.

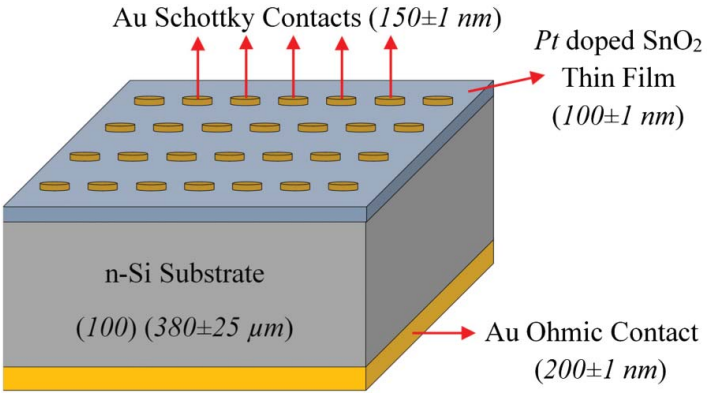


Figure 1. Schematic representation of the Au/Pt:SnO_2/n-Si/Au SBD.

It can be seen from Figure 2 that, there are Si (400), Si (200), SnO_2 (101), SnO_2 (310), SnO_2 (311), SnO_2 (202), SnO_2 (320), SnO (100) and Pt (220) peaks. That means the deposited SnO_2 thin films have polycrystalline structure.

As seen in Table 2, the structural parameters of the three samples such as the grain size (D), dislocation density (δ) and strain (ε) values were calculated. They were obtained from the equations given by

$$D = \frac{0.9\lambda}{\beta\cos\theta} \tag{1}$$

$$\delta = \frac{1}{D^2} \tag{2}$$

$$\varepsilon = \frac{1}{\tan\theta}\left(\frac{\lambda}{D\cos\theta} - \beta\right) \tag{3}$$

where λ is the X-ray wavelength (1.540 Å), θ is the peak angle value in the ω-2θ scans, hkl are the Miller indices and β is the full width at half maximum (FWHM) value of the SnO_2 peaks.[46]

It is seen from Table 2 that the grain size of the S001, which is the un-doped one, is lower than the others. On the contrary, S003 has the highest grain size and lowest dislocation density. It means that it has better crystallinity than the others. On the other hand, the FWHM of reflection peaks which is related with the grain size can be relevant to the crystal quality of the polycrystalline thin films.[47]

It can be seen from Figure 3 that, when the SnO_2 thin films were doped with Pt, the FWHM which is encoded in triangle decreased (except S002). It is expected from S003 that when the FWHM decreased, the grain size increased and dislocation density decreased and, thus, the crystallinity of the film increased. However, for the other samples, the crystallinity of the films was not increasing with the decreasing FWHM. The scientists observed similar phenomenon in 'Al doped Zinc Oxide' and 'Zn doped SnO_2' in the literature.[48,49]

Furthermore, the lattice spacing (d) which is between two different crystallographic planes and lattice parameters (a and c) of the tetragonal structure of SnO_2 can be

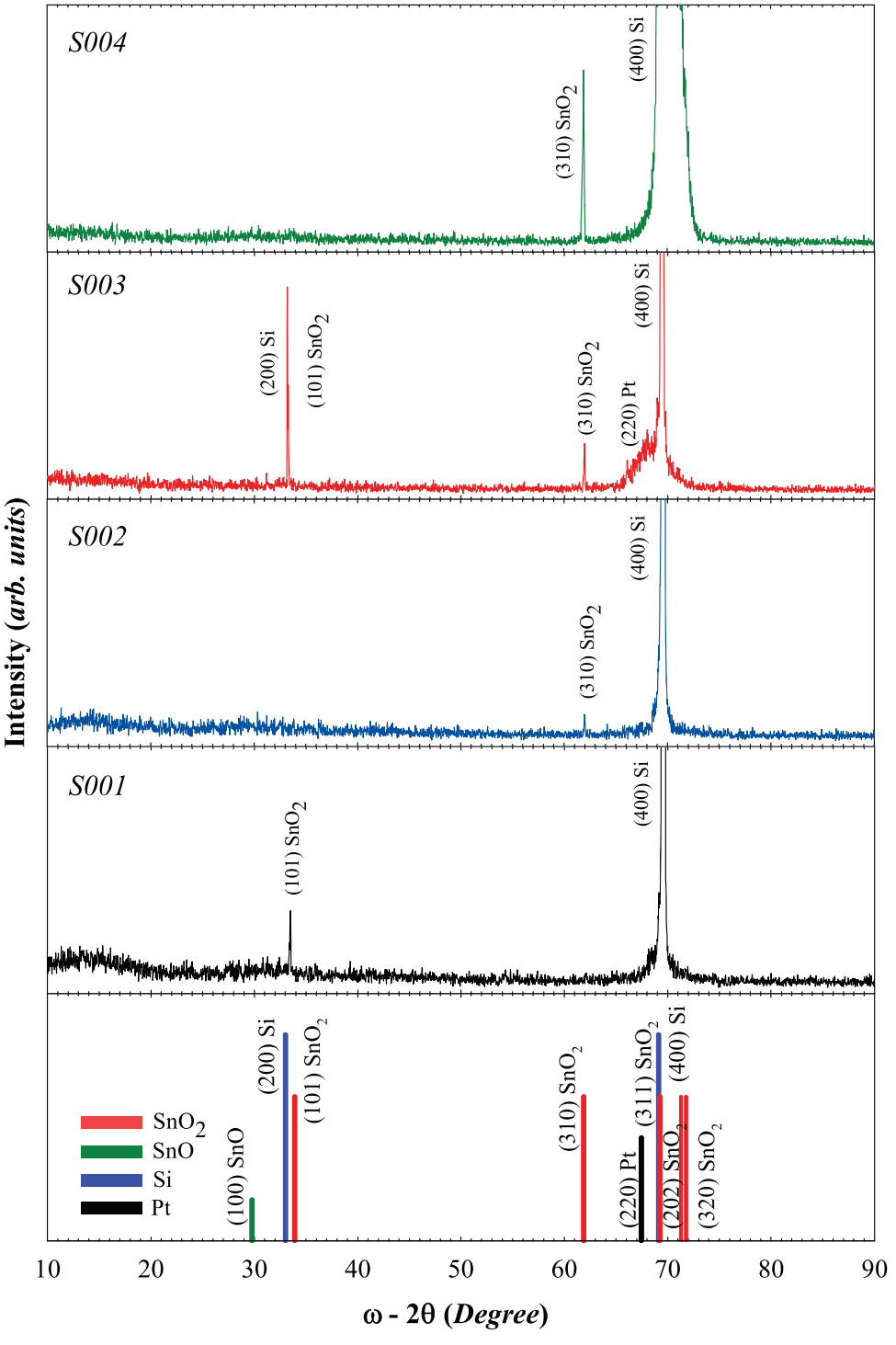


Figure 2. The ω-2θ XRD spectra of the samples.

Table 2. The structural parameters of the samples.

Sample	*hkl*	2θ (deg)	β (deg)	*D* (nm)	δ ($\times 10^9$ cm^{-2})	ε ($\times 10^{-4}$)
S001	101	33.440	0.089	92.993	0.115	0.575
S002	310	61.860	0.136	68.097	0.215	0.440
S003	101	33.200	0.047	175.259	0.032	0.307
S003	310	61.860	0.076	121.379	0.067	0.246
S004	310	61.860	0.087	105.722	0.089	0.283

determined by using Equations (4) and (5):

$$d = \frac{\lambda}{2\sin\theta} \tag{4}$$

$$\frac{1}{d^2} = \frac{h^2 + k^2}{a^2} + \frac{l^2}{c^2} \tag{5}$$

where h, k and l are the Miller indices of the reflection plane. Thus, the lattice parameters of S003 were found as $a = b = 4.739$ Å and $c = 3.279$ Å by using Equation (5) and related parameters. However, the well-known pure tetragonal SnO_2 has the lattice parameters as $a = b = 4.738$ Å and $c = 3.187$ Å.[49] Accordingly, there was a slight increase in the lattice constant of S003 compared to pure SnO_2, which indicates that some of the Pt^{4+} ions (with ionic radius 7.7 nm) incorporate into the Sn^{4+} sites of the SnO_2 (7.2 nm) lattice.[50]

3.2. Forward and reverse bias I–V characteristics

The experimental $I-V$ characteristics of Au/Pt:SnO_2/n-Si/Au SBDs were investigated at room temperature. The ln$I-V$ graph was drawn with obtained data and given in Figure 4.

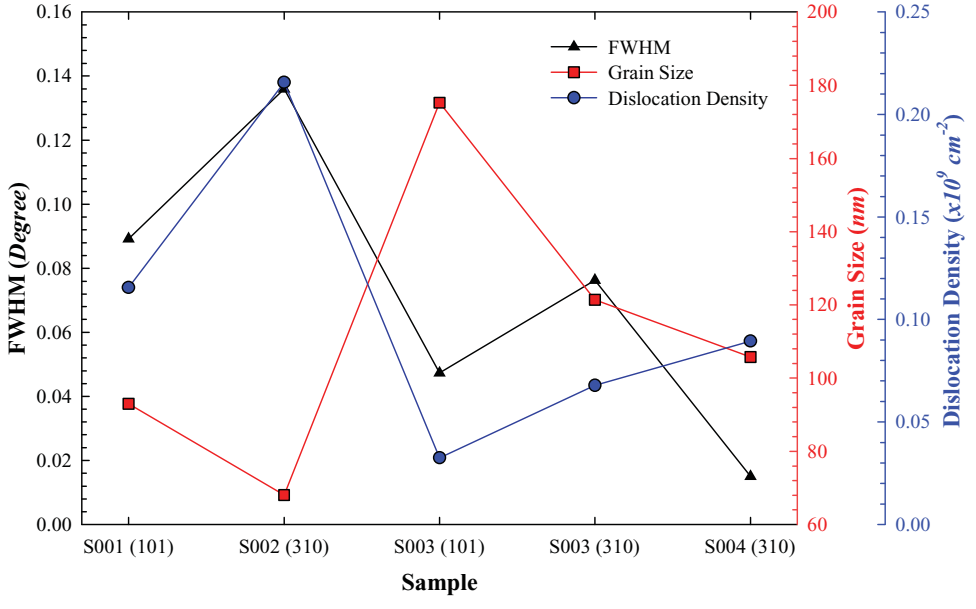


Figure 3. The calculated FWHM and grain sizes for the SnO_2 thin films.

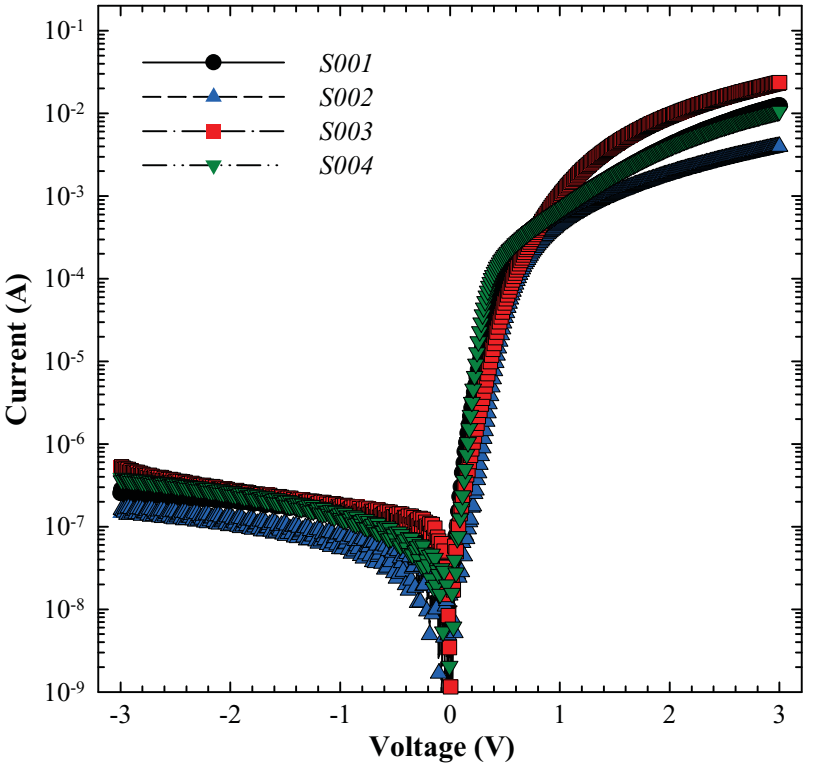


Figure 4. The semi-logarithmic plot of the ln*I*−*V* characteristics of SBDs.

In order to quantitatively analyse the SBDs, the standard thermionic emission theory was used as follows [51]:

$$I = I_0 \exp\left(\frac{q(V - IR_s)}{nkT}\right) \tag{6}$$

where q is the electronic charge, n is the ideality factor, k is the Boltzmann's constant and T is the absolute temperature in Kelvin. The term IR_s is the voltage drop across the series resistance of the diode. I_0 is the saturation current which is derived from the straight line intercept of ln$I$−V plot at zero bias voltage.[52] Thus, it is expected as

$$I_0 = AA^* T^2 \exp\left(-\frac{q\Phi_B}{kT}\right) \tag{7}$$

where Φ_B is the effective barrier height at zero bias, A is the rectifier contact area, A^* is the effective Richardson constant (112 A cm^{-2} K^{-2} for n-type Si).

The Φ_B was determined from the extrapolated I_0 and given by the relation:

$$\Phi_B = \frac{kT}{q} \ln\left(\frac{AA * T^2}{I_0}\right) \tag{8}$$

Table 3. The experimental $I-V$ results.

Parameters	Method	S001	S002	S003	S004
I_0 (μA)	ln$I-V$	76.80	4.81	44.00	11.60
N	ln$I-V$	2.30	2.21	2.70	1.44
	dV/d(ln$I$)	2.08	2.74	4.73	1.45
Φ_b (eV)	ln$I-V$	0.66	0.73	0.68	0.71
	$H(I)$	0.72	0.81	0.87	0.77
	$F(V)$	0.62	0.81	0.80	0.71
R_s (Ω)	dV/d(ln$I$)	977.63	891.63	225.48	1366.90
	$H(I)$	770.66	805.34	161.37	987.68
	$F(V)$	524.71	641.24	426.78	838.38
	R_i	242.36	749.78	127.36	280.94
R_{sh} (MΩ)	R_i	11.90	20.56	5.73	7.49

Additionally, n can be derived from the slope of linear region of the forward-bias ln$I-V$ plot.[53,54] It is given by

$$n = \frac{q}{kT}\left(\frac{\mathrm{d}V}{\mathrm{d}(\ln I)}\right) \tag{9}$$

As can be seen from Figure 4, the similar behaviour was observed due to the effects of some factors such as series resistance, interface states and interfacial layers. The linear region narrows and deviates from linearity.[55] The higher values of ideality factor can also indicate that an interfacial layer arises between metal and semiconductor. This layer can be formed either during surface preparation or fabrication processes.[56]

The experimental values of n and Φ_B were calculated as 2.30, 2.21, 2.70 and 1.44; 0.66, 0.73, 0.68 and 0.71 eV for S001, S002, S003 and S004 SBDs, respectively. These values were given in Table 3.

The n, Φ_B and R_s were also determined by using Cheung and Cheung functions.[57] These functions were given as

$$\frac{\mathrm{d}V}{\mathrm{d}(\ln I)} = n\left(\frac{kT}{q}\right) + IR_s \tag{10}$$

$$H(I) = V - n\left(\frac{kT}{q}\right)\ln\left(\frac{I}{AA * T^2}\right) = IR_s + n\Phi_B \tag{11}$$

Figures 5 and 6 show the experimental dV/d(ln$I$) vs. I and $H(I)$ vs. I plots for all the samples at room temperature. The plots give a straight line for the data of the downward curvature region in the forward-bias $I-V$. Therefore, the dV/d(ln$I$) vs. I plot's slope gives the R_s value, while the y-axis intercept gives the n value. The R_s and Φ_B values can be also obtained from $H(I)$-I plot with the same method.

Thus, the R_s and n values from dV/d(ln$I$) vs. I plot were found as 977.63, 891.63, 225.48 and 1366.90 Ω; 2.08, 2.74, 4.73 and 1.45 for S001, S002, S003 and S004 SBDs respectively. The R_s and Φ_B values from H(I)-I plot were found as 770.66, 805.34, 161.37 and 987.68 Ω; 0.72, 0.81, 0.87 and 0.77 eV for S001, S002, S003 and S004 SBDs, respectively. These values were given in Table 3. The R_s values obtained from dV/d(ln$I$)-I and $H(I)$-I plots were in agreement with each other.

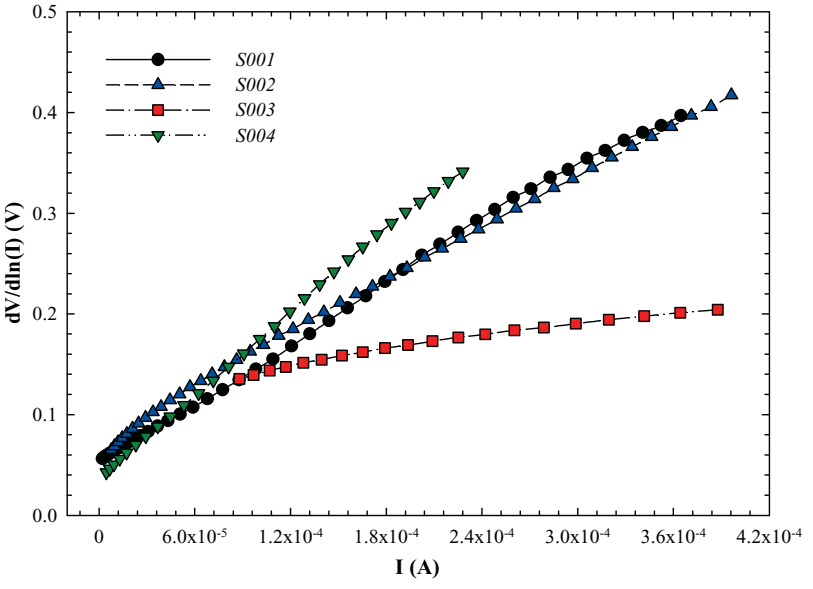


Figure 5. Experimental d*V*/d(ln*I*) vs. *I* plot of SBDs.

Additionally, the series resistance (R_s) and shunt resistance (R_{sh}) were obtained by using Ohm's law ($R_i = dV_i/dI_i$). The structure resistance (R_i)—applied bias voltage (V_i) graph was drawn with the experimental $I-V$ data and given in Figure 7.

It can be seen from Figure 7 that the structure resistance comes near to the maximum values in the reverse bias region, while it goes to the minimum at sufficiently

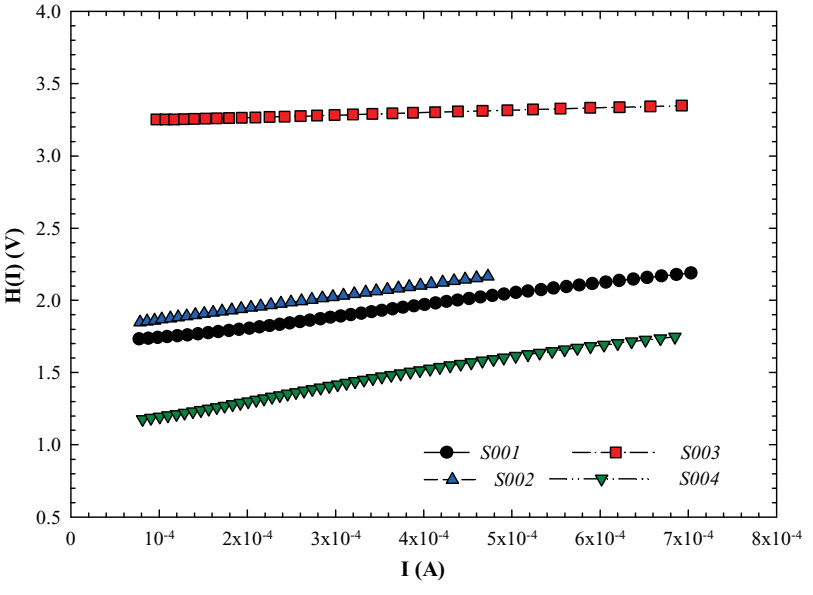


Figure 6. Experimental *H*(*I*) vs. *I* plot of SBDs.

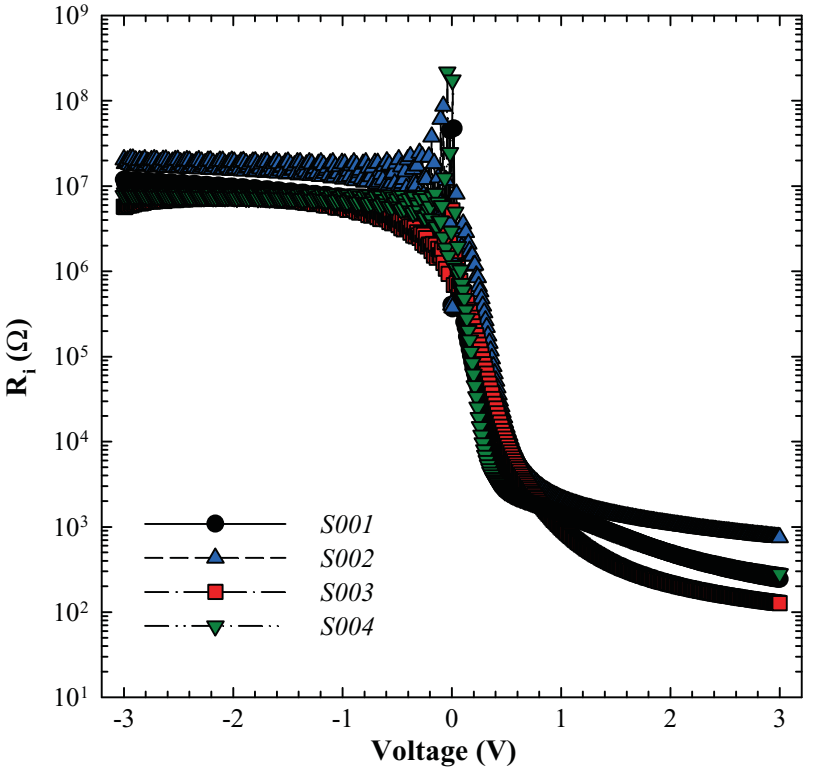


Figure 7. The R_i vs. V plot of SBDs.

high forward-bias voltage. The minimum and maximum regions correspond to the series and shunt resistances, respectively.[56] Thus, the values of R_s were found as 242.66, 749.78, 127.36 and 280.94 Ω for S001, S002, S003 and S004 SBDs, respectively. The values of R_{sh} were found as 11.90, 20.56, 5.73 and 7.49 MΩ for S001, S002, S003 and S004 SBDs, respectively. Therefore, it can be said that the R_{sh} values as high as possible and the R_s values as low as possible as expected. The obtained values were also given in Table 3.

For the comparison of results, Norde method which was modified by Lien was also used to determine R_s and Φ_B.[58,59] The $F(V)$ function was defined in this method as

$$F(V,\gamma) = \frac{V}{\gamma} - \frac{q}{kT}\ln\left(\frac{I(V)}{AA*T^2}\right) \tag{12}$$

where $I(V)$ is current value derived from $I-V$ curve and γ is a dimensionless integer greater than the ideality factor of diode.

When the minimum point of the $F(V)-V$ plot was determined, the value of Φ_B and R_s can be derived as following, where $F(V_{min})$ and V_{min} are coordinates of minimum point

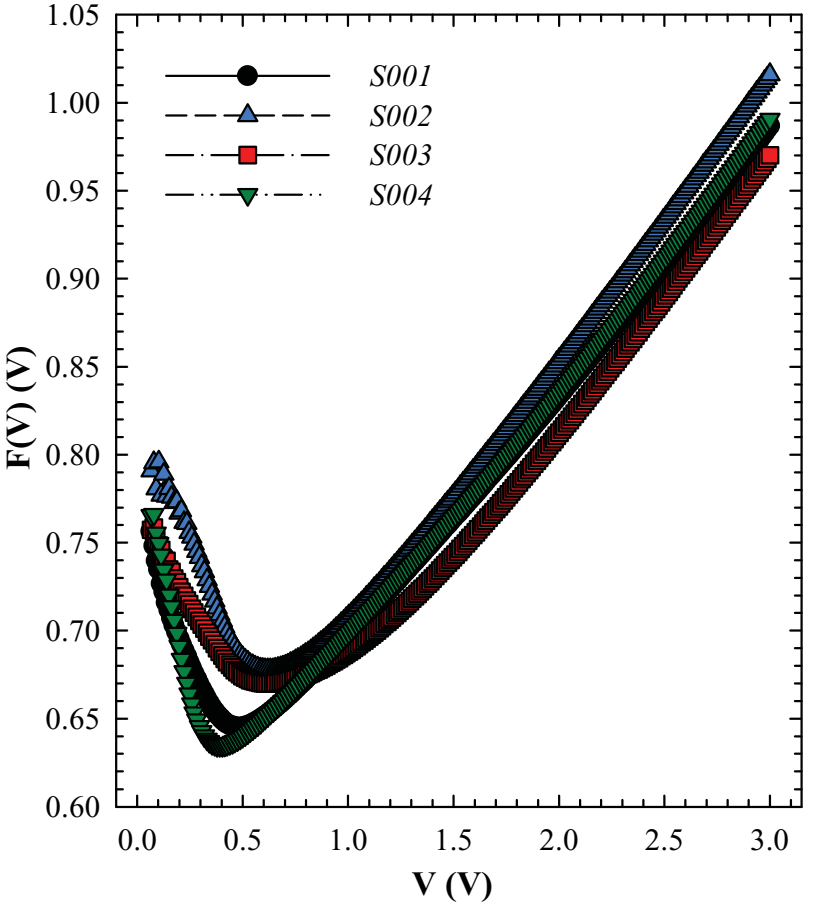


Figure 8. The *F*(*V*) vs. *V* plot of SBDs.

in the $F(V)-V$ plot shown in Figure 8.[59]

$$\Phi_B = F(V_{\min}) + \frac{V_{\min}}{\gamma} - \frac{kT}{q} \tag{13}$$

$$R_s = \frac{kT}{qI_{\min}}(\gamma - n) \tag{14}$$

where $I_{\min}$ is the value of the forward-bias current corresponding to $V_{\min}$.

The values of Φ_B obtained from Equation (13) were found as 0.62, 0.81, 0.80 and 0.71 eV for S001, S002, S003 and S004 SBDs, respectively. The values of R_s obtained from Equation (14) were found as 524.71, 641.24, 426.78 and 838.38 Ω for S001, S002, S003 and S004 SBDs, respectively. The obtained values were also given in Table 3.

3.3. Forward and reverse bias C–V and G/ω–V characteristics

The useful details about the structural changes and transport mechanism of the device can be generated by using the impedance spectroscopy. It is the most usable and preferable

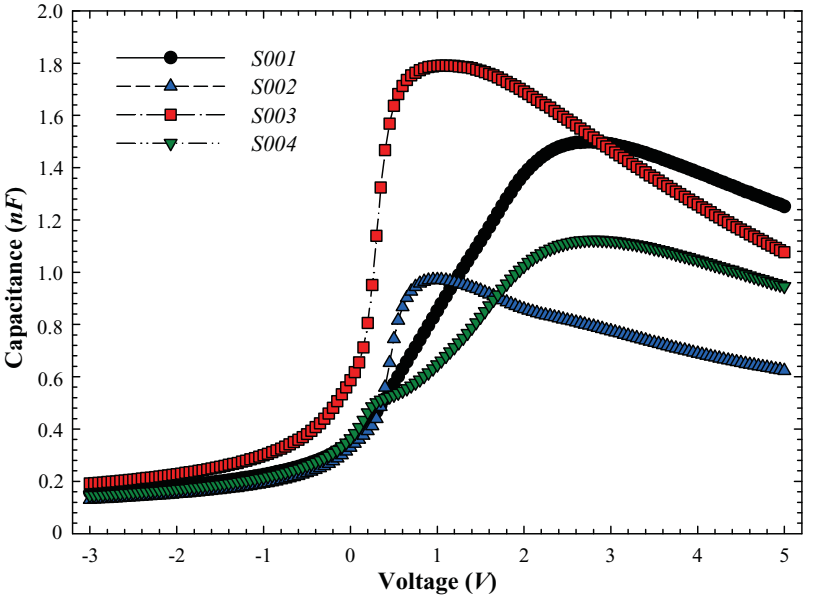


Figure 9. The forward and reverse bias $C-V$ characteristics of SBDs at 1 MHz.

technique to determine the dielectric properties of the nanomaterials.[60] The dielectric properties of nanomaterials are also very sensitive to the local electric field distribution in the sample. Therefore, the dielectric properties such as the dielectric constant (ε'), dielectric loss (ε'') and ac electrical conductivity (σ_{ac}) are very important for the selection of materials for device applications.

Figure 9 shows the experimental $C-V$ curves of the Au/Pt:SnO_2/n-Si/Au SBDs at 1 MHz frequency at room temperature. As shown in Figure 9, each $C-V$ curve has three regimes as an accumulation, depletion and inversion region. The voltage axis shifts due to the presence of interface states, at Si/SnO_2 interface, barrier inhomogeneous and oxide layer at the metal−semiconductor interface.[61] It can be said that the maximum capacitance was obtained with the S003 SBD.

Figure 10 shows the measured $G/\omega-V$ characteristics of SBDs at 1 MHz. It can be seen from Figure 10 that the values of conductance increased in the S003 SBD.

Additionally, the frequency dependence of dielectric constant (ε'), dielectric loss (ε'') and ac electrical conductivity (σ_{ac}) were evaluated from the measured $C-V$ and $G/\omega-V$ data in the frequency range of 100 Hz−1 MHz at room temperature.

The complex permittivity (ε^*) was determined using Equation (15) after measuring the capacitance and conductance of the samples.[51,52,62]

$$\varepsilon^* = \varepsilon' - i\varepsilon'' \tag{15}$$

where ε' is the real part of complex permittivity which describes the stored energy and ε'' is the imaginary part of complex permittivity which describes the dissipation energy and i is root square of −1. The complex permittivity formula can be rewritten as a function of capacitance and conductance. Thus, the frequency dependence of ε' and ε'' were

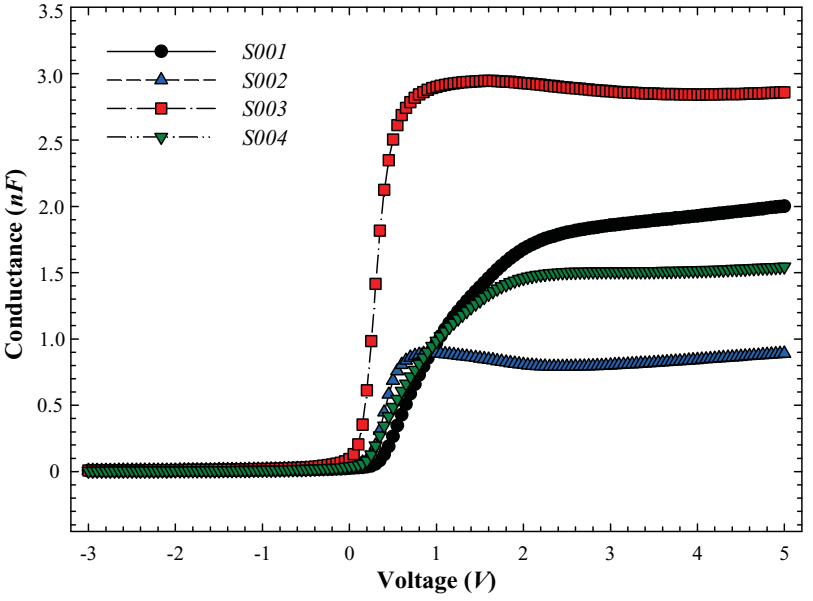


Figure 10. The forward and reverse bias $G/\omega-V$ characteristics of SBDs at 1 MHz.

determined by using Equations (16) and (17).[51,62]

$$\varepsilon' = \frac{C}{C_i} = \frac{Cd_i}{\varepsilon_0 A} \tag{16}$$

$$\varepsilon'' = \frac{G}{\omega C_i} = \frac{Gd_i}{\varepsilon_0 \omega A} \tag{17}$$

where C is the measured value of the capacitance of the device, d_i is the interfacial insulator layer thickness, ε_0 is the electric permittivity of free space ($\varepsilon_0 = 8.85 \times 10^{-14}$ F/cm) and A is the rectifier contact area of the diode in cm^{-2}. The maximal capacitance of the sample corresponds to the interfacial insulator layer capacitance $(C_i = \varepsilon' \varepsilon_0 A/d_i)$ in the strong accumulation region. Thus, from Equations (16) and (17), the quantity of tanδ can be expressed as follows [51,62]:

$$\tan\delta = \frac{\varepsilon''}{\varepsilon'} \tag{18}$$

Normally, the dielectric constant cannot be changed with the voltage frequency and temperature. However, it can be affected from polarisation mechanism which has a distinctive relaxation frequency. In addition, the dielectric properties of materials also depend on the structural properties and fabrication procedures of the sample.[63,64]

The room temperature frequency dependent dielectric constant graph was shown in Figure 11. It can be seen from Figure 11 that the dielectric constant of all devices decreases with increase in frequency. The observed features can be explained with Maxwell−Wagner type interfacial polarisation and Koops phenomenological theory.[65,66] It was also found that the dielectric constant of the Pt-doped SnO_2 devices exhibited lower

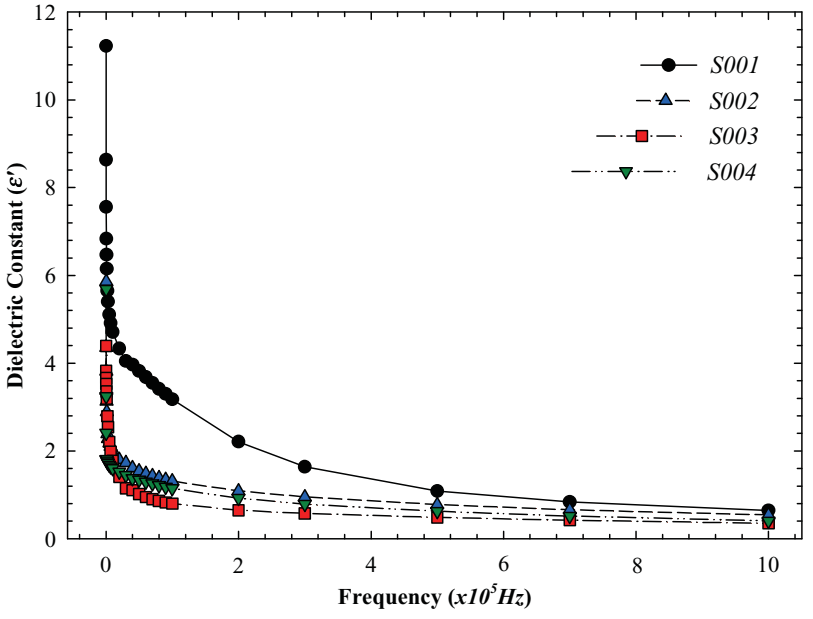


Figure 11. Dielectric constant plot of SBDs.

value than the pure SnO_2 diode. This decreasing may be due to the smaller dielectric polarisability and bigger ionic radius of dopant ions than the parent ions. This is also consistent with the wide bandgap band semiconductors have a lower dielectric constant.[67]

This behaviour of dielectric constant can also be clarified with the hopping model. The carrier exchange mechanism between different metal ions can impress upon the dielectric constant and ac conductivity. The hopping of electrons within the grain and grain boundaries can adapt to the applied ac field at lower frequencies. However, the electrons cannot follow the applied ac field at the higher frequencies. Thus, the electrons that are reaching the grain boundaries reduce; thus, the polarisation decreases which decreases the dielectric constant.[68]

In nanomaterials, inhomogeneity such as defects and space charge formation in the interphase layers can trap the current. Therefore, it can result in a dielectric loss. Figure 12 shows the room temperature frequency dependent dielectric loss graph. The dielectric loss also exhibits a similar behaviour with the dielectric constant. It was seen that the dielectric loss decreases with the increase in frequency and immediately after it remains constant for all Pt-doped SnO_2 samples.

It can be attributed to the Debye-like relaxation mechanism and the interfacial/space charge polarisation effect.[67,69] Thus, these types of materials can be used in high frequency device applications due to exhibition of a stable dielectric constant and dielectric loss behaviour at higher frequencies.

Figure 13 shows the variation of ac conductivity (σ_{ac}) values as a function of frequency for SBDs. It was observed that the ac conductivity was nearly constant up to 500 kHz and, thereafter, increases slightly in all samples. Additionally, the conductivity decreases with Pt-doping. This type of behaviour was also observed in 'Ni doped TiO_2 nanoparticles'.[70]

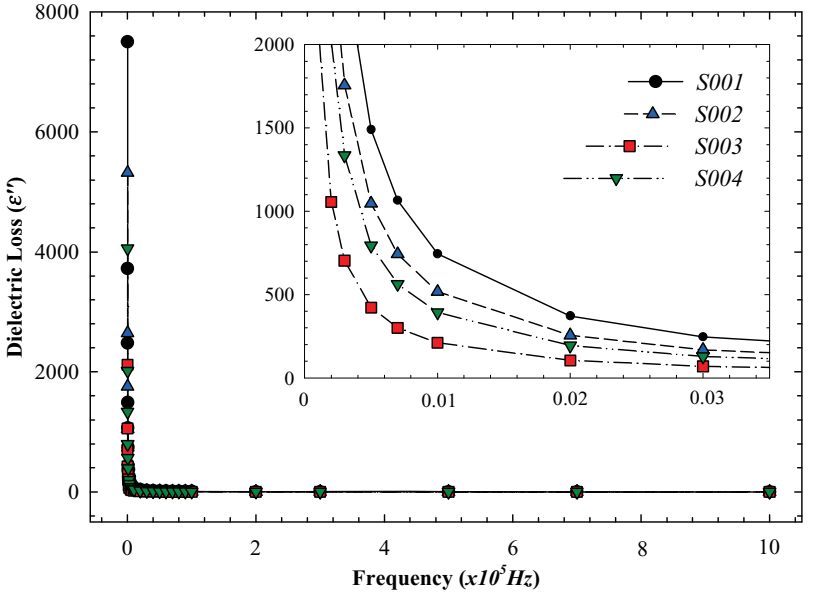


Figure 12. Dielectric loss plot of SBDs.

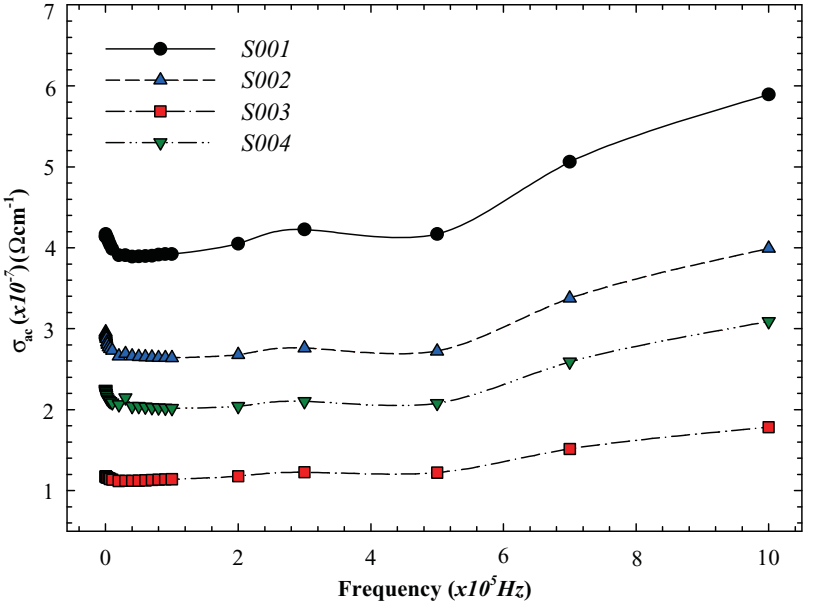


Figure 13. The variation of ac conductivity for SBDs.

It is also important to know whether the SBDs are n-type or p-type. This information can be obtained by calculating the capacitance between grains boundary, then by applying the following Mott−Schottky expression [71−73]:

$$\left(\frac{1}{C}-\frac{1}{2C_0}\right)^2=\frac{2}{q\varepsilon_s\varepsilon_0 N_d}(\Phi_B+V) \tag{19}$$

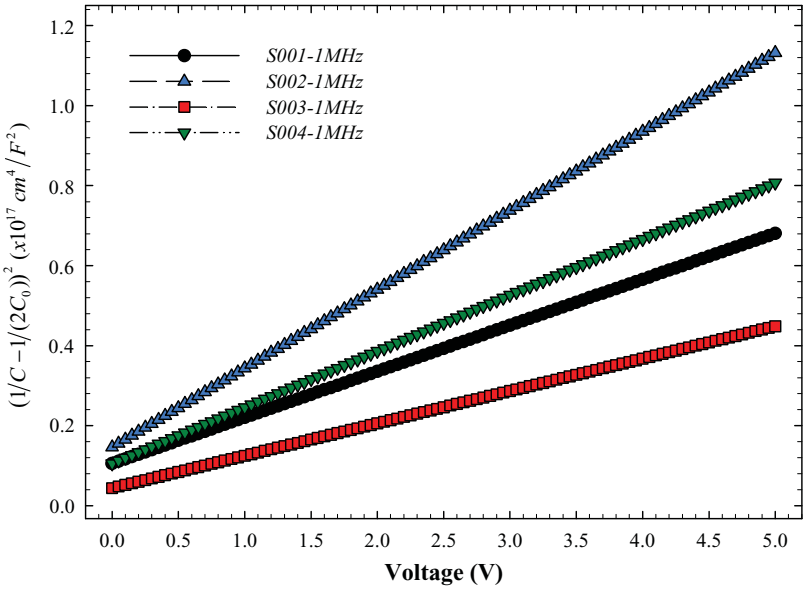


Figure 14. $\left(1/C-1/(2C_0)\right)^2-V$ graph for SBDs.

where

$$\frac{1}{C_0}=2\left(\frac{2\Phi_B}{q\varepsilon_s\varepsilon_0 N_d}\right)^{1/2} \tag{20}$$

and q is the electronic charge, ε_s is the dielectric constant of n-type Si (11.8 ε_0), ε_0 is the dielectric constant of vacuum (8.85 × 10^{-14} F/cm), N_D is the doping concentration and V is the applied voltage.

Thus, the plotting $(1/C-1/(2C_0))^2$versus applied voltage according to Equation (19) should yield a straight line. Figure 14 shows the relation between $(1/C-1/(2C_0))^2=f(V)$ as function of applied voltage. When the slope of $(1/C-1/(2C_0))^2-V$ graph is positive, hence, the semiconductor device is n-type. Similarly, when the slope of $(1/C-1/(2C_0))^2-V$ graph is negative, the semiconductor device is p-type.[71]

It can be seen from Figure 14 that the slope of $(1/C-1/(2C_0))^2-V$ graph is linear and positive, hence, the SBDs are also n-type. The results are also given in Table 4.

Figure 15 shows the reciprocal of the squared capacitance per unit area as a function of the bias at constant frequency (1 MHz). It can be seen from Figure 15 that the $C^{-2}-V$ plots were linear. This linearity of the curves can be indicated with the uniformity of the donor concentration in the depletion region. It can be also said that the interface states cannot follow ac signal at high frequency regions.[52]

Table 4. The electrical parameters of SBDs obtained from $C^{-2}-V$ data at 1 MHz.

Sample	Type	V_0 (V)	V_d (V)	N_D (cm^{-3})	E_F (eV)	W_D (cm)	$\Delta\Phi_B$ (meV)	Φ_B (eV)
S001	n	0.705	0.731	1.041×10^{15}	0.197	9.572×10^{-5}	13.648	0.914
S002	n	0.516	0.542	6.070×10^{14}	0.211	1.079×10^{-4}	11.066	0.741
S003	n	0.345	0.370	1.483×10^{15}	0.187	5.712×10^{-5}	13.949	0.544
S004	n	0.534	0.542	8.525×10^{14}	0.202	9.260×10^{-5}	10.956	0.751

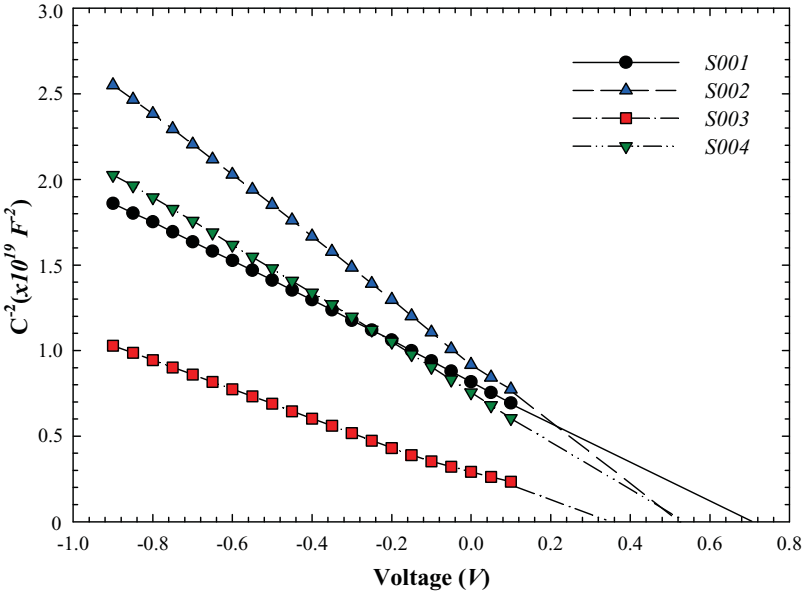


Figure 15. $C^{-2}-V$ characteristics for SBDs at 1 MHz.

It can be possible that the doping concentration (N_D), Fermi energy level (E_F), depletion layer width (W_D), built-in voltage at zero bias (V_0), diffusion potential at zero bias (V_d), image force barrier lowering ($\Delta\Phi_B$) and barrier height (Φ_B ($C-V$)) can be obtained from the $C^{-2}-V$ characteristics of SBDs at 1 MHz by using the following equations.

If the $C-V$ measurements at 1 MHz are considered, the depletion layer capacitance in SBD can be expressed as [51,52]

$$C^{-2} = \frac{2(V_0 + V_R)}{q\varepsilon_s\varepsilon_0 A^2 N_D} \tag{21}$$

$$N_D = \frac{2}{q\varepsilon_s\varepsilon_0 A^2 \left(\frac{d(C^{-2})}{dV}\right)} \tag{22}$$

where q is the electronic charge, ε_s is the dielectric constant of n-type Si (11.8 ε_0), ε_0 is the dielectric constant of vacuum (8.85×10^{-14} F/cm), A is the diode area, N_D is the doping concentration, V_R is the reverse bias voltage and V_0 is the built-in voltage at zero bias. It can be determined from the extrapolation of $C^{-2}-V$ plot and given as

$$V_0 = V_d - \frac{kT}{q} \tag{23}$$

The Φ_B ($C-V$) values were also calculated by using the following relation:

$$\Phi_B(C-V) = V_0 + \frac{kT}{q} + E_F - \Delta\Phi_B \tag{24}$$

where $\Delta\Phi_B$ is the image force barrier lowering and given by [74]

$$\Delta\Phi_B = \left(\frac{qE_m}{4\pi\varepsilon_s\varepsilon_0}\right)^{1/2} \tag{25}$$

where E_m is the maximum electric field. E_m was obtained from the following relation:

$$E_m = \left(\frac{2qN_D V_d}{\varepsilon_s\varepsilon_0}\right)^{1/2} \tag{26}$$

E_F is obtained from

$$E_F = \frac{kT}{q}\ln\left(\frac{N_C}{N_D}\right) \tag{27}$$

N_C is the effective density of states in the semiconductor conductance band which is obtained from

$$N_C = 4.82 \times 10^{15} T^{3/2}\left(\frac{m_e^*}{m_0}\right)^{3/2} \tag{28}$$

where m_e^* is the effective mass of the electron, m_0 is the rest mass of the electron.

Additionally, the W_D was also derived by using Equation (29) [75]:

$$W_D = \left(\frac{2\varepsilon_s\varepsilon_0 V_d}{qN_D}\right)^{1/2} \tag{29}$$

The obtained values of V_0, V_d, N_D, E_F, W_D, $\Delta\Phi_B$ and Φ_B ($C-V$) were presented in Table 4. The similar results have been reported in the literature.[61]

In general, n-type metal oxide nanomaterials are also shaped due to oxygen vacancies, which change the crystallographic structure and lead to a donor level below but close to the conduction band.[76] It means that the Fermi energy level (E_F) is also low when it is doped. It can be seen from Table 4 that the Fermi energy level (E_F), built-in voltage at zero bias (V_0), diffusion potential at zero bias (V_d) and barrier height (Φ_B ($C-V$)) of S003 are lower than the other SBDs.

4. Conclusion

This study investigated the properties of the SnO_2 thin films depended on Pt doping concentrations. In order to investigate the Pt doping effect, the Pt sputter power was varied as 0 (un-doped), 2, 5 and 7 W. Thus, the samples were called as S001 (un-doped), S002 (2 W Pt-doped), S003 (5 W Pt-doped) and S004 (7 W Pt-doped). The structural and electrical characteristics of the samples were obtained by XRD, $I-V$, $C-V$ and $G/\omega-V$ measurements. XRD results show that S003 has better crystallinity, which is depended on the FWHM, grain size and dislocation density, than the others. It can be seen from the

electrical results that the Pt-doped samples have lower Φ_B and higher R_{sh} values. It was also observed that the ε' and ε'' show a similar behaviour, they decrease and, thereafter, remain constant for all the samples. Additionally, ε' and ε'' decrease with Pt-doping. The σ_{ac} was nearly constant up to 500 kHz and, thereafter, increases slightly in all samples. σ_{ac} decreases with Pt-doping.

In summary, the structural and electrical characteristics of the SnO_2 samples were significantly affected by the Pt-doping. Although the preferable features of all doped samples, S003 has come into prominence due to its better properties. As a result, it can be said that S003 type SnO_2 thin films can be more convenient for SnO_2 based electro-optic and electrochemical device applications.

Disclosure statement

No potential conflict of interest was reported by the authors.

Funding

This work is supported by the Ministry of Development of Turkey [project number 2011K120290]; Ministry of Science, Industry and Technology of Turkey [project number 0633.STZ.2014].

ORCID

Tarık Asar http://orcid.org/0000-0002-2430-0599

References

[1] Bargougui R, Oueslati A, Schmerber G, et al. Structural, optical and electrical properties of Zn-doped SnO_2 nanoparticles synthesized by the co-precipitation technique. J Mater Sci Mater Electron. 2014;25:2066–2071. doi: 10.1007/s10854-014-1841-2.

[2] Gui T, Hao L, Wang J, et al. Structure and features of SnO_2 thin films prepared by RF reactive sputtering. Chin Opt Lett. 2010;8:134–136. doi: 10.3788/COL201008S1.0134.SnO.

[3] Kamble VB, Bhat SV, Umarji AM. Investigating thermal stability of structural defects and its effect on d0 ferromagnetism in undoped SnO_2. J Appl Phys. 2013;113:244307. doi: 10.1063/1.4812382.

[4] Ginley DS, Bright C. Transparent conducting oxides. MRS Bull. 2000;25:15–18. doi: 10.1557/mrs2000.256.

[5] Chopra KL, Major S, Pandya DK. Transparent conductors – a status review. Thin Solid Films. 1983;102:1–46. doi: 10.1016/0040-6090(83)90256-0.

[6] Snaith HJ, Ducati C. SnO2-based dye-sensitized hybrid solar cells exhibiting near unity absorbed photon-to-electron conversion efficiency. Nano Lett. 2010;10:1259–1265. doi: 10.1021/nl903809r.

[7] McDowell MG, Sanderson RJ, Hill IG. Combinatorial study of zinc tin oxide thin-film transistors. Appl Phys Lett. 2008;92:2007–2009. doi: 013502\r10.1063/1.2828862.

[8] Li Y, Yin W, Deng R, et al. Realizing a SnO_2-based ultraviolet light-emitting diode via breaking the dipole-forbidden rule. NPG Asia Mater. 2012;4:e30. doi: 10.1038/am.2012.56.

[9] Isono T, Fukuda T, Nakagawa K, et al. Highly conductive SnO_2 thin films for flat-panel displays. J Soc Inf Disp. 2007;15:161–166. doi: 10.1889/1.2709738.

[10] Nelli P, Faglia G, Sberveglieri G, et al. The aging effect on SnO_2 Au thin film sensors: electrical and structural characterization. Thin Solid Films. 2000;371:249–253.

[11] Hagemeyer A, Hogan Z, Schlichter M, et al. High surface area tin oxide. Appl Catal A Gen. 2007;317:139−148. doi: 10.1016/j.apcata.2006.09.040.
[12] Paek SM, Yoo E, Honma I. Enhanced cyclic performance and lithium storage capacity of SnO_2/graphene nanoporous electrodes with three-dimensionally delaminated flexible structure. Nano Lett. 2009;9:72−75. doi: 10.1021/nl802484w.
[13] Bernardi MIB, Soledade LE, Santos IA, et al. Influence of the concentration of Sb_2O_3 and the viscosity of the precursor solution on the electrical and optical properties of SnO_2 thin films produced by the Pechini method. Thin Solid Films. 2002;405:228−233. doi: 10.1016/S0040-6090(01)01770-9.
[14] Yan J, Khoo E, Sumboja A, et al. Facile coating of manganese oxide on tin oxide nanowires with high-performance capacitive behavior. ACS Nano. 2010;4:4247−4255. doi: 10.1021/nn100592d.
[15] Scott JF. High-dielectric constant thin films for dynamic random access memories (Dram). Annu Rev Mater Sci. 1998;28:79−100. doi: 10.1146/annurev.matsci.28.1.79.
[16] Bose AC, Kalpana D, Thangadurai P, et al. Synthesis and characterization of nanocrystalline SnO_2 and fabrication of lithium cell using nano-SnO_2. J Power Sources. 2002;107:138−141. doi: 10.1016/S0378-7753(01)00995-8.
[17] Borse RY, Garde AS. Electrical and gas sensing properties of SnO_2 thick film resistors prepared by screen-printing method. Sensors Transducers. 2008;97:64−73.
[18] Hudaya C, Jeon BJ, Lee JK. High thermal performance of SnO_2:F thin transparent heaters with scattered metal nanodots. ACS Appl Mater Interfaces. 2015;7:57−61. doi: 10.1021/am507497u.
[19] Luo G, Shen Q, Li Q, et al. Corrosion behavior of SnO_2-based electrode ceramics in soda-lime glass liquid. IOP Conf Ser Mater Sci Eng. 2011;18:202025. doi: 10.1088/1757-899X/18/20/202025.
[20] Gu F, Wang SF, Lü MK, et al. Photoluminescence properties of SnO_2 nanoparticles synthesized by Sol−Gel method. J Phys Chem B. 2004;108:8119−8123. doi: 10.1021/jp036741e.
[21] Giulio MD, Micocci G, Serra A, et al. Characteristics of reactively sputtered Pt-SnO_2 thin films for CO gas sensors. J Vac Sci Technol A. 1996;14:2215−2219. doi: 10.1116/1.580049.
[22] Kim KH, Park CG. Electrical properties and gas sensing behavior of SnO_2 films prepared by chemical vapor deposition. J Electrochem Soc. 1991;138:2408−2412. doi: 10.1149/1.2085986.
[23] Schweizer-Berberich M, Zheng JG, Weimar U, et al. The effect of Pt and Pd surface doping on the response of nanocrystalline tin dioxide gas sensors to CO. Sensors Actuators B Chem. 1996;31:71−75. doi: 10.1016/0925-4005(96)80018-9.
[24] Kim H, Auyeung RCY, Piqué A. Transparent conducting F-doped SnO_2 thin films grown by pulsed laser deposition. Thin Solid Films. 2008;516:5052−5056. doi: 10.1016/j.tsf.2007.11.079.
[25] Pena J, Perez-Pariente J, Vallet-Regi M. Textural properties of nanocrystalline tin oxide obtained by spray pyrolysis. J Mater Chem. 2003;13:2290−2296. doi: 10.1039/b304830f.
[26] Du F, Guo Z, Li G. Hydrothermal synthesis of SnO_2 hollow microspheres. Mater Lett. 2005;59:2563−2565. doi: http://dx.doi.org/10.1016/j.matlet.2005.03.046.
[27] Manorama SV, Gopal Reddy CV, Rao VJ. Tin dioxide nanoparticles prepared by sol-gel method for an improved hydrogen sulfide sensor. Nanostruct Mater. 1999;11:643−649. doi: 10.1016/S0965-9773(99)00352-9.
[28] Li Y, Peng R, Xiu X, et al. Growth of SnO_2 nanoparticles via thermal evaporation method. Superlattices Microstruct. 2011;50:511−516. doi: 10.1016/j.spmi.2011.08.013.
[29] Tian ZM, Yuan SL, He JH, et al. Structure and magnetic properties in Mn doped SnO2 nanoparticles synthesized by chemical co-precipitation method. J Alloys Compd. 2008;466:26−30. doi: 10.1016/j.jallcom.2007.11.054.
[30] Gaggiotti G, Galdikas A, Kaciulis S, et al. Temperature dependencies of sensitivity and surface chemical composition of SnO_x gas sensors. Sensors Actuators B Chem. 1995;25:516−519. doi: 10.1016/0925-4005(95)85111-9.
[31] Matko I, Gaidi M, Hazemann JL, et al. Electrical properties under polluting gas (CO) of Pt- and Pd-doped polycrystalline SnO_2 thin films: analysis of the metal aggregate size effect. Sensors Actuators B Chem. 1999;59:210−215. doi: 10.1016/S0925-4005(99)00222-1.
[32] Cheong H-W, Choi J-J, Kim HP, et al. The role of additives in tin dioxide-based gas sensors. Sensors Actuators B Chem. 1992;9:227−231. doi: http://dx.doi.org/10.1016/0925-4005(92)80221-I.

[33] Tadeev AV, Delabouglise G, Labeau M. Influence of Pd and Pt additives on the microstructural and electrical properties of SnO_2-based sensors. Mater Sci Eng B. 1998;57:76–83. doi: 10.1016/S0921-5107(98)00251-7.
[34] Azam A, Ahmed AS, Chaman M, et al. Investigation of electrical properties of Mn doped tin oxide nanoparticles using impedance spectroscopy. J Appl Phys. 2010;108:094329. doi: 10.1063/1.3506691.
[35] Azam A, Ahmed AS, Ansari MS, et al. Study of electrical properties of nickel doped SnO_2 ceramic nanoparticles. J Alloys Compd. 2010;506:237–242. doi: 10.1016/j.jallcom.2010.06.184.
[36] Chang S-S, Jo MS. Luminescence properties of Eu-doped SnO_2. Ceram Int. 2007;33:511–514. doi: 10.1016/j.ceramint.2005.10.021.
[37] Shimizu Y, Egashira M. Basic aspects and challenges of semiconductor gas sensors. MRS Bull. 1999;24:18–24. doi: 10.1557/S0883769400052465.
[38] Schierbaum KD, Weimar U, Göpel W, et al. Conductance, work function and catalytic activity of SnO_2-based gas sensors. Sensors Actuators B Chem. 1991;3:205–214. doi: 10.1016/0925-4005(91)80007-7.
[39] Sangaletti L, Depero LE, Allieri B, et al. Oxidation of Sn thin films to SnO_2 micro-Raman mapping and X-ray diffraction studies. J Mater Res. 1998;13:2457–2460.
[40] Kılıç Ç, Zunger A. Origins of coexistence of conductivity and transparency in SnO_2. Phys Rev Lett. 2002;88:095501. doi: 10.1103/PhysRevLett.88.095501.
[41] Zhang Y, Yu K, Li G, et al. Synthesis and field emission of patterned SnO_2 nanoflowers. Mater Lett. 2006;60:3109–3112. doi: 10.1016/j.matlet.2006.02.053.
[42] Mehraj S, Ansari MS. Structural, dielectric and complex impedance properties of Cd doped SnO_2 nanoparticles. J Nanoeng Nanomanuf. 2013;3:229–236. doi: 10.1166/jnan.2013.1137.
[43] Chenari HM, Hassanzadeh A, Golzan MM, et al. Frequency dependence of ultrahigh dielectric constant of novel synthesized SnO_2 nanoparticles thick films. Curr Appl Phys. 2011;11:409–413. doi: 10.1016/j.cap.2010.08.011.
[44] Acciarri M, Canevali C, Mari CM, et al. Nanocrystalline SnO_2-based thin films obtained by sol-gel route: a morphological and structural investigation. Chem Mater. 2003;15:2646–2650. doi: 10.1021/cm031002w.
[45] Şafak-Asar Y, Asar T, Altındal Ş, et al. Investigation of dielectric relaxation and ac electrical conductivity using impedance spectroscopy method in (AuZn)/TiO_2/p-GaAs(110) Schottky barrier diodes. J Alloys Compd. 2015;628:442–449. doi: 10.1016/j.jallcom.2014.12.170.
[46] Asar T, Özçelik S. Barrier enhancement of Ge MSM IR photodetector with Ge layer optimization. Superlattices Microstruct. 2015;88:685–694. doi: 10.1016/j.spmi.2015.10.034.
[47] Maniv S, Zangvil A. Controlled texture of reactively rf-sputtered ZnO thin films. J Appl Phys. 1978;49:2787.
[48] Fu E-G, Zhuang D-M, Zhang G, et al. Properties of transparent conductive ZnO:Al thin films prepared by magnetron sputtering. Microelectron J. 2004;35:383–387. doi: 10.1016/S0026-2692(03)00251-9.
[49] Ni J, Zhao X, Zhao J. P-type transparent conducting SnO_2:Zn film derived from thermal diffusion of Zn/SnO2/Zn multilayer thin films. Surf Coat Technol. 2012;206:4356–4361. doi: 10.1016/j.surfcoat.2012.04.031.
[50] Khairy M, Mohamed MM. SnO(β-Bi_2O_3)/$Bi_2Sn_2O_7$ nanohybrids doped with Pt and Pd nanoparticles: applications in visible light photocatalysis, electrical conductivity and dye-sensitized solar cells. Phys Chem Chem Phys. 2015;17:21716–21728. doi: 10.1039/C5CP02066B.
[51] Rhoderick EH, Williams RH. Metal-semiconductor contacts. 2nd ed. Oxford: Clarendon Press; 1988.
[52] Sze SM. Physics of semiconductor devices. 3rd ed. Hoboken (NJ): John Wiley & Sons. Inc.; 2007.
[53] Card HC, Rhoderick EH. Studies of tunnel MOS diodes I. Interface effects in silicon Schottky diodes. J Phys D Appl Phys. 1971;4:1589–1601. doi: 10.1088/0022-3727/4/10/319.
[54] Kınacı B, Özen Y, Kızılkaya K, et al. Effect of alloy composition on structural, optical and morphological properties and electrical characteristics of $Ga_xIn_{1-x}P$/GaAs structure. J Mater Sci Mater Electron. 2013;24:1375–1381. doi: 10.1007/s10854-012-0937-9.

[55] Kinaci B, Asar T, Çetin SŞ, et al. Electrical characterization of Au/ZnO /TiO2/n-Si and (Ni/Au)/ZnO/TiO_2/n-Si Schottky diodes by using current-voltage measurements. J Optoelectron Adv Mater. 2012;14:959−963.
[56] Taşçıoğlu İ, Altındal Ş, Polat İ, et al. The effect of metal work function on the barrier height of metal/CdS/SnO_2/In−Ga structures. Curr Appl Phys. 2013;13:1306−1310. doi: 10.1016/j.cap.2013.04.010.
[57] Cheung SK, Cheung NW. Extraction of Schottky diode parameters from forward current-voltage characteristics. Appl Phys Lett. 1986;49:85−87. doi: 10.1063/1.97359.
[58] Norde H. A modified forward I-V plot for Schottky diodes with high series resistance. J Appl Phys. 1979;50:5052−5053. doi: 10.1063/1.325607.
[59] Lien CD, So FCT, Nicolet MA. An improved forward I-V method for nonideal Schottky diodes with high series resistance. IEEE Trans Electron Devices. 1984;ED-31:1502−1503. doi: 10.1109/T-ED.1984.21739.
[60] Şafak Asar Y, Asar T, Altındal Ş, et al. Dielectric spectroscopy studies and ac electrical conductivity on (AuZn)/TiO_2/p-GaAs(110) MIS structures. Philos Mag. 2015;95:2885−2898. doi: 10.1080/14786435.2015.1081301.
[61] Tataroğlu A, Altındal Ş. Characterization of interface states at Au/SnO_2/n-Si (MOS) structures. Vacuum. 2008;82:1203−1207. doi: 10.1016/j.vacuum.2007.12.014.
[62] Nicollian EH, Brews JR. MOS (metal oxide semiconductor) physics and technology. Hoboken (NJ): Wiley Interscience Publication; 1982.
[63] Ulrich RK, Schaper LW. Integrated passive component technology. Hoboken (NJ): Wiley - IEEE; 2003.
[64] Blythe AR, Bloor D. Electrical properties of polymers. Cambridge: Cambridge University Press; 1979.
[65] Maxwell JC. Electricity and magnetism. Oxford: Clarendon Press; 1892.
[66] Koops CG. On the dispersion of resistivity and dielectric constant of some semiconductors at audio frequencies. Phys Rev. 1951;83:121−124. doi: 10.1103/PhysRev.83.121.
[67] Pandian SK, Karthik K, Sureshkumar K, et al. Effect of Mn-doping on structural, optical, and dielectric properties of SnO_2 nanoparticles by coprecipitation method. Mater Manuf Process. 2012;27:130−134. doi: 10.1080/10426914.2011.557130.
[68] Mehraj S, Ansari MS, Alimuddin. Structural, electrical and magnetic properties of (Fe, Co) co-doped SnO_2 diluted magnetic semiconductor nanostructures. Phys E Low-Dimens Syst. Nanostruct. 2015;65:84−92. doi: 10.1016/j.physe.2014.08.016.
[69] Yang H, Lin Y, Wang F, et al. Chemical synthesis of $K_{0.5}Na_{0.5}NbO_3$ ceramics and their electrical properties. Mater Manuf Process. 2008;23:489−493. doi: 10.1080/10426910802104070.
[70] Karthik K, Pandian SK, Jaya NV. Effect of nickel doping on structural, optical and electrical properties of TiO_2 nanoparticles by sol−gel method. Appl Surf Sci. 2010;256:6829−6833. doi: 10.1016/j.apsusc.2010.04.096.
[71] Batal MA, Jneed FH. Tin oxide n-type semiconductor inverted to p- type semiconductor prepared by sol-gel method. Energy Procedia. 2011;6:1−10. doi: 10.1016/j.egypro.2011.05.001.
[72] Mukae K, Tsuda K, Nagasawa I. Capacitance-vs-voltage characteristics of ZnO varistors. J Appl Phys. 1979;50:4475−4476. doi: 10.1063/1.326411.
[73] Fernández-Hevia D, de Frutos J, Caballero AC, et al. Mott−Schottky behavior of strongly pinned double Schottky barriers and characterization of ceramic varistors. J Appl Phys. 2002;92:2890−2898. doi: 10.1063/1.1498968.
[74] De Visschere P. Image forces and MIS Schottky barriers. Solid State Electron. 1986;29:873−875. doi: 10.1016/0038-1101(86)90006-7.
[75] Tataroğlu A. Comparative study of the electrical properties of Au/n-Si (MS) and Au/Si_3N_4/n-Si (MIS) Schottky diodes. Chin Phys B. 2013;22:068402. doi: 10.1088/1674-1056/22/6/068402.
[76] Shao S, Wu H, Jiang F, et al. Regulable switching from p- to n-type behavior of ordered nanoporous Pt-SnO_2 thin films with enhanced room temperature toluene sensing performance. RSC Adv. 2016;6:22878−22888. doi: 10.1039/C5RA24736E.